




**Atomic and electronic structure of an epitaxial Nb<sub>2</sub>O<sub>3</sub> honeycomb monolayer on Au(111)**

Shuqiu Wang <sup>1</sup>, Jacek Goniakowski,<sup>2</sup> Claudine Noguera,<sup>2</sup> and Martin R. Castell <sup>1,\*</sup>  
<sup>1</sup>*Department of Materials, University of Oxford, Parks Road, Oxford, OX1 3PH, United Kingdom*  
<sup>2</sup>*CNRS-Sorbonne Université, UMR 7588, INSP, F-75005 Paris, France*

 (Received 18 April 2019; revised manuscript received 2 August 2019; published 9 September 2019)

The experimental discovery and theoretical analysis of an epitaxial ( $2 \times 2$ ) honeycomb Nb<sub>2</sub>O<sub>3</sub> monolayer on a Au(111) surface is reported. The oxide monolayer is grown by Nb deposition and subsequent annealing in an oxidizing atmosphere. Scanning tunneling microscopy (STM) images show that the films form a well-ordered honeycomb lattice, and low energy electron diffraction patterns confirm that the films adopt a ( $2 \times 2$ ) periodicity with respect to the Au(111) substrate. Density functional theory (DFT) modeling shows that the Nb atoms are located in Au(111) threefold hollow sites and the O atoms are located in on-top positions. DFT also demonstrates the existence of a strong interfacial interaction characterized by a large electron transfer towards the Au substrate, an increase of the Nb oxidation state, and substantial film rumpling. High-resolution STM images, supported by simulations, are able to discriminate between Nb atoms adsorbed in fcc or hcp hollow sites on the Au(111) substrate.

DOI: [10.1103/PhysRevB.100.125408](https://doi.org/10.1103/PhysRevB.100.125408)

**I. INTRODUCTION**

Oxide monolayers consist of one layer of atoms or polyhedron units [1], and are of technological interest in the fields of catalysis and corrosion [2,3]. They are also effective model systems for metal-oxide interfaces that are relevant in the process of high-temperature oxide encapsulation of noble metal catalysts. In fundamental materials research, oxide monolayers are attractive systems because they have properties that do not exist in bulk oxides such as modified crystallography and stoichiometry as well as unusual electronic and magnetic behavior.

The structures of oxide monolayers are determined by the nature of the oxide and the interactions with the substrate. The cations in transition metal oxides can adopt a variety of oxidation states which can result in a range of bulk crystal stoichiometries and structures (e.g., FeO, Fe<sub>3</sub>O<sub>4</sub>, and Fe<sub>2</sub>O<sub>3</sub>). Analogously, monolayer films of transition metal oxides can also form a myriad of complex surface structures. For example, in the system of TiO<sub>x</sub> films supported on Pt(111), the formal oxidation states of the Ti ions range from +2 to +4 and the stoichiometry of the TiO<sub>x</sub> films ranges from TiO to TiO<sub>2</sub>. TiO<sub>x</sub> films show a series of kagomé, zigzag, wagon-wheel, rectangular, and hexagonal structures [4–6]. Lattice mismatch at the oxide-metal interface results in compressive or tensile strain in the overlayer structures. The structures accommodate strain through the formation of islands [7], dislocations [8], and domain structures [4].

Oxide monolayers may grow as a relaxed layer that forms a coincidence structure with the substrate and these films show a moiré pattern. Alternatively, they may be constrained

to match the substrate lattice as experimentally observed in many oxide monolayers grown on metals, for example in systems such as NiO(100)–( $1 \times 1$ )/Ag(100) [9], WO<sub>3</sub>– $c(2 \times 2)$ /Pd(100) [10], CoO(100)– $c(4 \times 2)$ /Pd(100) [11], V<sub>2</sub>O<sub>3</sub> ( $2 \times 2$ )/Pd(111) [12], Ti<sub>2</sub>O<sub>3</sub> ( $2 \times 2$ )/Au(111) [13–18], and FeWO<sub>3</sub> ( $2 \times 2$ )/Pt(111) [19]. Among various structures of oxide monolayers, the M<sub>2</sub>O<sub>3</sub> honeycomb ( $2 \times 2$ ) structure has been extensively studied. It has been theoretically modeled as a freestanding film of V<sub>2</sub>O<sub>3</sub>, Ti<sub>2</sub>O<sub>3</sub>, Cr<sub>2</sub>O<sub>3</sub>, Fe<sub>2</sub>O<sub>3</sub> [20], and Nb<sub>2</sub>O<sub>3</sub> [21]. Calculations of the electronic structure of the freestanding Nb<sub>2</sub>O<sub>3</sub> monolayer revealed topologically protected edge states, which survive upon deposition on a MoS<sub>2</sub> substrate [21]. However, this is unlikely to be the case for honeycomb M<sub>2</sub>O<sub>3</sub> structures synthesized on metals due to a stronger oxide/substrate interaction. Simulations of such systems include V<sub>2</sub>O<sub>3</sub> on Pd(111) [22,23], Ti<sub>2</sub>O<sub>3</sub> [5] and FeWO<sub>3</sub> [19] on Pt(111), and M<sub>2</sub>O<sub>3</sub> (M = Sc, Ti, V, Cr, Mn, Fe, Co, Ni) [16,23,24] or Cu<sub>3</sub>O<sub>2</sub> [25] on Au(111). The honeycomb structure is a fully coordinated network consisting of hexagonal rings which can be used as a template for the adsorption of metal atoms, and a novel ternary oxide of Ba<sub>x</sub>Ti<sub>2</sub>O<sub>3</sub> was grown using this method [14].

Here we report the experimental discovery of a well-ordered ( $2 \times 2$ ) Nb<sub>2</sub>O<sub>3</sub> honeycomb monolayer on the Au(111) surface. Its large-scale crystal structure is characterized with scanning tunneling microscopy (STM) and low energy electron diffraction (LEED), its fine atomic structure is analyzed via high-resolution STM images, and its electronic properties are determined using density functional theory (DFT). We show that the observed monolayer structure is consistent with a strong Nb<sub>2</sub>O<sub>3</sub>–Au(111) interaction and substantial film rumpling which helps accommodate the lattice mismatch between a hypothetical freestanding oxide film and the Au substrate.

\*martin.castell@materials.ox.ac.uk

## II. METHODS

### A. Experimental methods

The experiments were performed in an ultrahigh vacuum (UHV) system at a base pressure of  $10^{-8}$  Pa. Measurements were carried out in a JEOL JSTM 4500XT instrument which includes STM and LEED analysis facilities. Polished Au single crystals (SurfaceNet GmbH, Germany) cut to reveal the (111) termination were treated by repeated sputtering and annealing cycles. Mica-supported Au(111) single crystals (Agilent Technologies, UK) were also used as substrates. Both types of Au(111) substrates were sputtered by  $\text{Ar}^+$  ions (0.75–1 keV) and UHV annealed to 600 °C for 1.5 h resulting in the herringbone reconstruction. Nb vapor was deposited using an e-beam evaporator (Oxford Applied Research EGN4) from a 99.99% pure Nb rod supplied by Goodfellow, UK. The samples were then annealed in  $10^{-6}$  Pa  $\text{O}_2$  at 600 °C for 1 h to create the  $(2 \times 2)$  niobium oxide ultrathin films. Constant current STM images were produced at room temperature using etched tungsten tips. Most STM images presented in the paper are the result of multiple frame averaging (MFA) using a software package called SMART ALIGN with the general method described in Ref. [26] and the specific application to STM described in Ref. [27]. Detailed image processing methods are provided in the Supplemental Material [28].

### B. Theoretical calculations

All computational results were obtained within the plane-wave density functional approach, using the spin-polarized gradient-corrected PW91 exchange-correlation functional [29] and the projector-augmented wave method [30] implemented in VASP [31,32]. Simulated STM images were obtained within the Tersoff-Hamann approximation [33]. Atomic charges were estimated according to Bader's method [34,35].

Calculations on the supported oxide film were performed in a  $(1 \times 1) - \text{Nb}_2\text{O}_3 // (2 \times 2) - \text{Au}(111)$  coincidence cell, with the  $\text{Nb}_2\text{O}_3$  film deposited on one side of the Au(111) slab composed of six atomic Au layers. Periodic slab images were separated by more than 10 Å of vacuum, and dipole corrections were used to eliminate the remaining spurious interactions between periodic replicas. The in-plane lattice parameters were fixed at the experimental gold lattice parameter of 4.08 Å and the reciprocal space was sampled with a fine  $(14 \times 14 \times 1)$  Monkhorst-Pack grid. The atomic positions of all the ions in the  $\text{Nb}_2\text{O}_3$  film and of the gold atoms in the two surface layers were fully optimized, while those of the remaining Au atoms were relaxed only in the direction normal to the surface (threshold on forces = 0.001 eV/Å).

Interestingly, a refinement of the oxide electronic structure within the DFT +  $U$  approximation [36] ( $U - J = 1.5$  eV for Nb) and taking into account the dispersion forces [37,38], results in only a relatively small impact on the film structure ( $d_{\text{Au-Nb}}$  distances shorten by 0.02 Å, and film rumpling increases by 0.02 Å), despite a non-negligible reinforcement of the interaction strength with the gold substrate (adhesion energy increases by 0.3 eV/ $\text{Nb}_2\text{O}_3$ ) and of the interface charge transfer (by 0.1  $e/\text{Nb}_2\text{O}_3$ ).

## III. EXPERIMENTAL RESULTS AND DISCUSSION

### A. Crystal structure of niobium oxide monolayers

Figure 1 shows STM images of the evolution of the surface structures upon increasing the coverage from 0.16 monolayer (ML, where 1 ML coverage corresponds to a Au surface fully covered by one layer of niobium oxide) to 1.83 ML. Figure 1(a) shows a Au(111) surface following the deposition of Nb and subsequent oxidation to achieve a coverage of 0.16 ML. Niobium oxide on Au(111) forms a film structure with a honeycomb lattice as well as island structures with triangular shapes. Bare patches of the Au(111) substrate (dark areas) coexist with the oxide islands. The herringbone reconstruction is lifted underneath the oxide film and distorted in the bare regions. As the coverage is increased from 0.16 to 0.85 ML, several separately nucleated honeycomb domains meet and transform into continuous domains [Figs. 1(a)–1(d)]. The surface structures are dominated by honeycomb units and triangular islands. Some defects are seen in the honeycomb lattice, such as Nb vacancies [bottom right in Fig. 1(c)] and domain boundaries [top left in Fig. 1(c)]. Domain boundaries are formed to accommodate the epitaxial offset between two domains. Depositing more Nb on a  $\text{NbO}_x$  surface of 0.85 ML coverage and annealing the surface in oxygen increases the oxide coverage to 1.83 MLs [Fig. 1(e)]. Disordered structures grow on top of the honeycomb structures and triangular islands. Depositing more Nb onto the  $\text{NbO}_x$  surface of 1.83 MLs and annealing the surface in oxygen increases the oxide coverage to 2.2 MLs. The honeycomb structure is no longer observed and the surface is covered by disordered structures. We were not able to discover the processing parameters required to create ordered films beyond 1-ML coverage.

The LEED pattern taken at 0.85 ML coverage [Fig. 1(f)] indicates a commensurate  $(2 \times 2)$  superstructure (indicated by an orange rhombus) with respect to the Au(111) substrate (white rhombus), which corresponds to an overlayer lattice constant of 5.77 Å. The unit cell of the oxide film is aligned along the  $[1\bar{1}0]$  directions of the Au(111) substrate.

Annealing the niobium oxide surface covered by 0.9-ML honeycomb at 800 °C in UHV and  $10^{-6}$  Pa  $\text{O}_2$  barely affects the coverage or the crystal structure of the honeycomb monolayer. Annealing the honeycomb surface at 400 °C in  $10^{-4}$  Pa  $\text{O}_2$  also has little effect. This stability is in contrast to that of the honeycomb monolayers of  $\text{V}_2\text{O}_3$  and  $\text{Ti}_2\text{O}_3$  which transform into more oxidized phases under elevated temperatures and higher oxygen pressures [4,12,13].

### B. Atomic structure of niobium oxide honeycomb films

Figure 2 shows the atomic structure of the  $(2 \times 2)$  oxide phase. Experimental STM images with two different tip terminations show bright protrusions at the vertices [Fig. 2(a)] or the bridge sites [Fig. 2(c)] of the honeycomb network. The hexagonal network has a measured average periodicity of  $5.8 \pm 0.1$  Å which corresponds to the  $(2 \times 2)$  periodicity of Au(111) surface, in agreement with the LEED pattern [Fig. 1(f)].

The atomic structure and crystallographic orientation with respect to the Au(111) surface of the niobium oxide honeycomb phase are similar to those observed for the

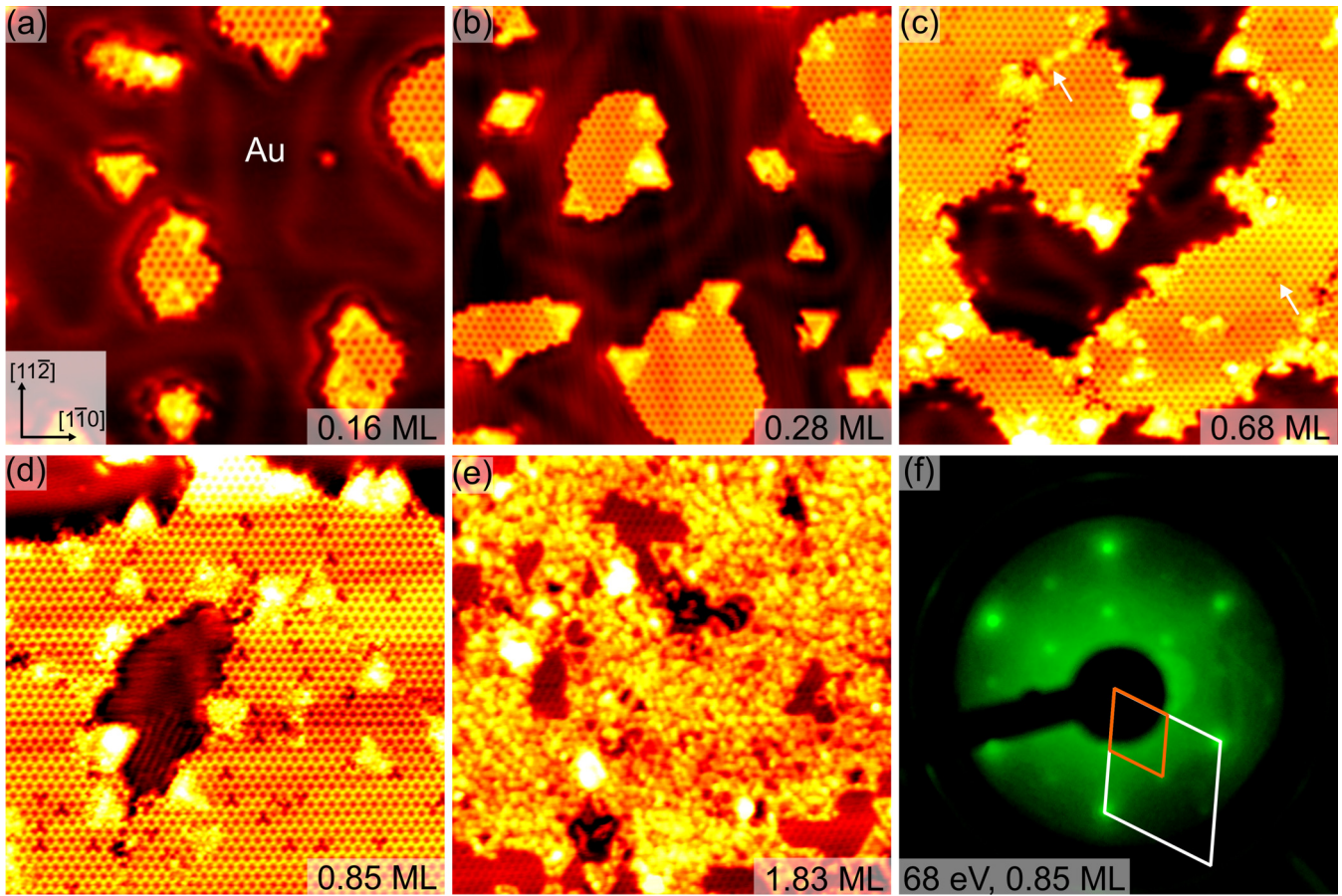


FIG. 1. Overview of niobium oxide grown on Au(111) at increasing coverage. STM images of niobium oxides at (a) 0.16 ML, (b) 0.28 ML, (c) 0.68 ML, (d) 0.85 ML, and (e) 1.83 ML. Atomic vacancies and domain boundaries are indicated by arrows in (c). (f) LEED pattern (taken at 68 eV) showing a  $(2 \times 2)$  superstructure (orange rhombus) on a Au(111) surface (white rhombus) covered by 0.85 ML of oxide. The STM images from (a)–(d) are generated from 19, 71, 14, and 8 frames using MFA to enhance the signal-to-noise ratio, as described in the Supplemental Material [28]. The experimental STM parameters are (a) image width 21.0 nm,  $V_s = 0.45$  V, and  $I_t = 0.26$  nA; (b) image width 27.0 nm,  $V_s = 0.4$ –1 V, and  $I_t = 0.26$  nA; (c) image width 24.7 nm,  $V_s = 1$  V, and  $I_t = 0.16$  nA; (d) image width 24.0 nm,  $V_s = 1$  V, and  $I_t = 0.18$  nA; (e) image width 30.0 nm,  $V_s = 1$  V, and  $I_t = 0.25$  nA.

epitaxial honeycomb  $(2 \times 2)\text{Ti}_2\text{O}_3/\text{Au}(111)$  system with the Ti atoms located in Au(111) threefold hollow sites and the O atoms located in on-top positions [14]. We adopt the previous interpretation for the  $\text{Ti}_2\text{O}_3$  monolayer directly and assign the Nb atoms to bright protrusions imaged in Fig. 2(a), and O atoms in Fig. 2(c). The structural model of the niobium oxide honeycomb monolayer is shown in Fig. 2(e). Each unit cell [highlighted in Figs. 2(a), 2(c), and 2(e)] contains two Nb atoms and three O atoms. Each Nb atom is coordinated with three O atoms and each O atom is coordinated with two Nb atoms. The stoichiometry of the honeycomb phase is  $\text{Nb}_2\text{O}_3$ . Image simulations [Figs. 2(b) and 2(d)] are in good agreement with the experimental STM images. The theoretical calculations are discussed in detail in Sec. IV.

### C. Observation of Nb atoms in hcp and fcc adsorption sites

After image processing using MFA, STM images show fine surface features that cannot be observed in single frames [27]. The STM image [left of Fig. 3(a)], averaged over 176 frames without other image filtering, shows that half of the Nb sites, marked as *A* sites are marginally brighter than the other half,

marked as *B* sites. The differences between *A* and *B* sites are visualized in the right panel of Fig. 3(a) using another look-up table that has been chosen for maximum contrast. The height difference can also be seen in the profile taken along the highlighted *A*-*B* pair in Fig. 3(a) and shown in Fig. 3(b). Measurements of 66 *A*-*B* site pairs were taken from this image resulting in an average height difference ( $\Delta h$ ) of  $1.83 \pm 0.20$  pm.

The measurements of  $\Delta h$  have only small variations within each image, but show more significant average differences depending on tip termination and imaging parameters. Measurements of multiple *A*-*B* site pairs were taken from single STM images resulting in a variety of values for  $\Delta h$ . Eighteen  $\Delta h$  averages plotted against the sample bias are shown in Fig. 3(d). The data sets are separated into two regions of lower (filled squares, classified as Dataset 1) and higher (open circles, classified as Dataset 2) values of  $\Delta h$ . This suggests that in our experiments there are two generally stable apical tip configurations. The majority of the data sets fall in the lower region (filled squares), which ranges from 1.83 to 5.87 pm with a preponderance of values around 3 pm. The decrease of  $\Delta h$  can be approximated by an inverse



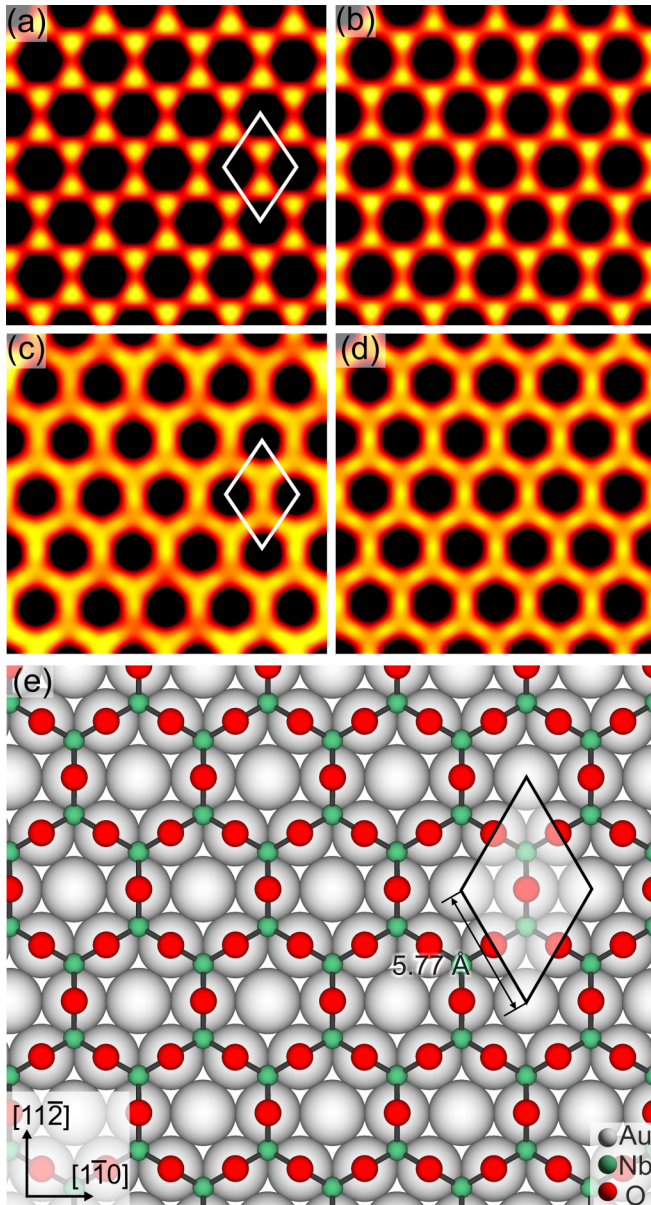


FIG. 2. Pristine  $\text{Nb}_2\text{O}_3$  ( $2 \times 2$ ) honeycomb structure. (a) Experimental empty states STM image (averaged from 290 frames, image width 2.9 nm,  $V_s = 0.8$  V, and  $I_t = 0.16$  nA). (b) DFT simulation of the empty states STM image ( $E - E_F = +1$  V, distance from the center of the first Au substrate plane is 6.0 Å). (c) Experimental filled states STM image (averaged from 46 raw frames, image width 2.9 nm,  $V_s = -0.5$  V and  $I_t = 0.18$  nA). (d) DFT simulation of the filled states STM image ( $E - E_F = -0.5$  V, distance from the center of the first Au substrate plane is 6.0 Å). (e) A schematic of the  $\text{Nb}_2\text{O}_3$  monolayer with a honeycomb lattice on Au(111). Nb atoms (green) are threefold coordinated with O atoms (red). Au atoms are in gray. A ( $2 \times 2$ ) Au(111) unit cell is highlighted in (a), (c), and (e).

exponential fit with the sample bias. An increase in sample bias will generally result in an increase in the tip-sample separation with an associated reduction of atomic corrugation height in the images. The three data points above 6 pm (open circles) are not included in the red line fit and are probably due to a different apical tip termination [39].

The origin of the difference of the height of the A sites and B sites in Fig. 3(a) can be explained by analyzing the structure of the  $\text{Nb}_2\text{O}_3$  overlayer. Figure 3(c) is a schematic showing a Au(111) surface where the top three atomic Au layers can be seen with the location of the Nb atoms on the left and the full  $\text{Nb}_2\text{O}_3$  overlayer on the right. The Nb atoms (green balls) are located in threefold hollow sites on the Au(111) surface, and the O atoms (red balls) are located on the “top” sites (white). There are two types of threefold hollow sites, namely hcp sites (light gray) and fcc sites (dark gray), as indicated in Fig. 3(c). The structure of the overlayer results in half of the Nb atoms sitting in the hcp sites, and the other half in fcc sites. A DFT simulated STM image [in the top right corner of Fig. 3(a)] is in good agreement with the experimental STM image. In simulations, the Nb atoms located on the hcp sites are marginally brighter than the ones on the fcc sites. It is according to this simulation that we assign the A and B sites to the hcp and fcc locations, respectively.

#### IV. THEORETICAL RESULTS AND DISCUSSION

##### A. Atomic structure of $\text{Nb}_2\text{O}_3$ ( $2 \times 2$ ) honeycomb monolayer on Au(111)

Atomistic simulations confirm that Nb atoms preferentially occupy the hollow (fcc and hcp) surface sites, whereas oxygen atoms, which bridge two neighboring cations, are located in on-top surface Au sites [Fig. 3(c)]. There is a slightly different local environment of the fcc and hcp Au hollow adsorption sites and this results in the Nb cations in the hcp sites being located 1 pm further away from the surface than those in the fcc sites. Compared to the hypothetical calculated freestanding honeycomb monolayer which is perfectly flat [Fig. 4(b)], the Au-supported  $\text{Nb}_2\text{O}_3$  film has significant structural polarization (rumpling)  $\delta_{\text{Z}_{\text{Nb-O}}} = 0.93$  Å, with the anions relaxing outwards and the cations approaching the Au(111) surface [Fig. 4(a)]. Such film rumpling helps accommodate the lattice mismatch between the gold substrate and the freestanding honeycomb monolayer [ $a_{\text{Nb}_2\text{O}_3} \sim 6.67$  Å,  $a_{\text{Au}}(2 \times 2) = 5.77$  Å] while allowing a quasinegligible contraction of the cation-anion distance ( $d_{\text{Nb-O}} = 1.91$  Å) with respect to the freestanding reference ( $d_{\text{Nb-O}} = 1.93$  Å).

##### B. Adhesion energy

The oxide-metal interaction strength can be estimated by the adhesion energy  $E_{\text{adh}} = -[E(\text{Nb}_2\text{O}_3/\text{Au}) - E(\text{Nb}_2\text{O}_3) - E(\text{Au})]$ , where  $E(\text{Nb}_2\text{O}_3/\text{Au})$ ,  $E(\text{Nb}_2\text{O}_3)$ , and  $E(\text{Au})$  are the total energies of the oxide-covered slab, a freestanding fully relaxed oxide layer, and the bare gold slab, respectively. The calculated adhesion energy is  $2.34$  J/m<sup>2</sup> (4.2 eV per  $\text{Nb}_2\text{O}_3$  formula unit or  $14.6$  eV/nm<sup>2</sup>), typical of strongly interacting metal/oxide interfaces or other honeycomb transition metal oxides on Au(111) [24,40]. This number can be decomposed into two contributions, namely the elastic energy necessary to constrain the lattice parameter of the freestanding honeycomb monolayer to that of the gold substrate ( $-1.8$  eV) and the oxide-metal interaction energy gained when bringing the constrained oxide film into contact with the Au(111) surface (6.0 eV). Despite the large lattice mismatch between the

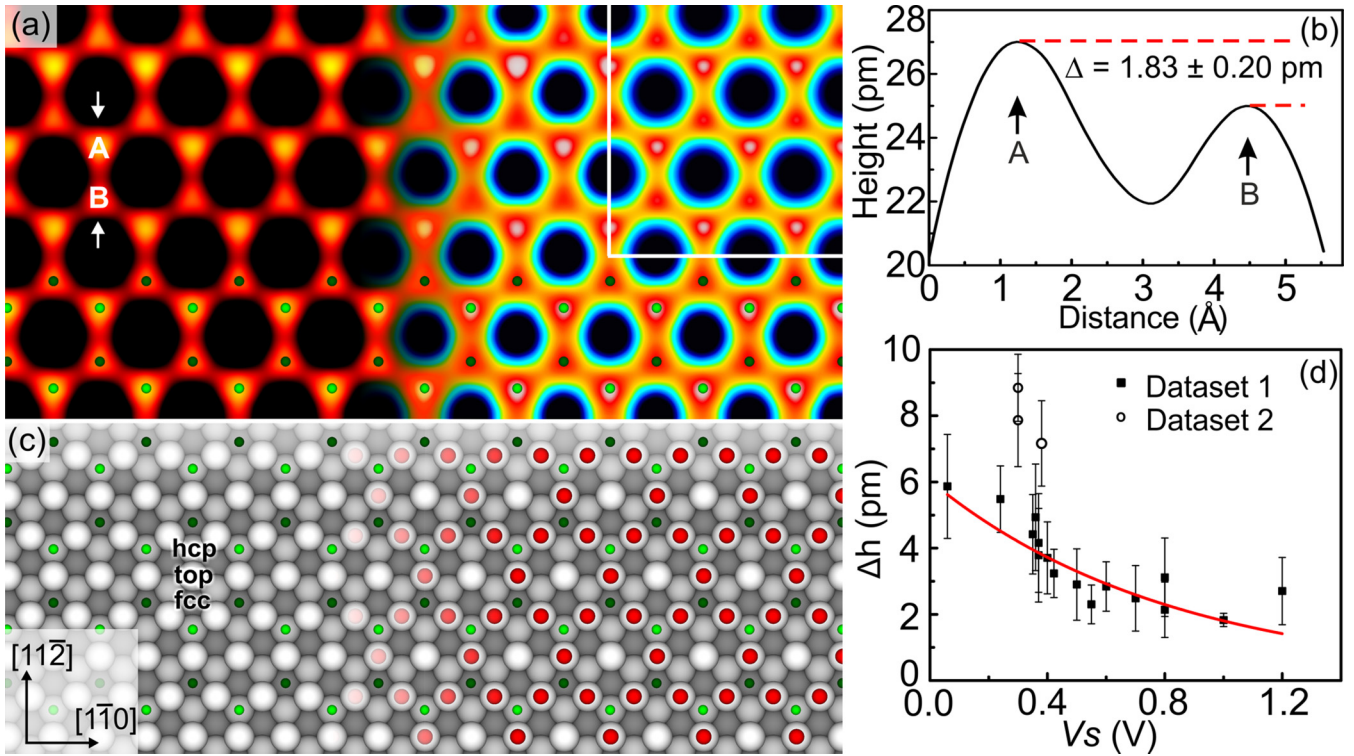


FIG. 3. STM image and detailed analysis of the  $(2 \times 2)$  honeycomb  $\text{Nb}_2\text{O}_3$  monolayer structure on Au(111). (a) (Left) experimental empty states STM image (averaged from 176 raw frames, image width 5.2 nm,  $V_s = 1.0$  V and  $I_t = 0.18$  nA). (Right) the same data as in the left part but with a different look-up table that has been chosen for maximum contrast. The top right inset shows a calculated STM image showing that the hcp sites appear brighter than fcc sites ( $E - E_F = +1$  V, distance from the center of the first Au substrate plane is 6.0 Å). (b) Line profile from the highlighted  $A$ - $B$  pair in (a) showing the 1.83 pm difference in height of the  $A$  and  $B$  sites. (c) Epitaxial model of the  $(2 \times 2)$  honeycomb  $\text{Nb}_2\text{O}_3$  monolayer on Au(111) with top (white), hcp (light gray), and fcc (dark gray) sites indicated. Nb atoms located on the hcp and fcc sites are in light and dark green, respectively. O atoms are shown in red. (d) Plot of  $A$ - $B$  pair height differences ( $\Delta h$ ) vs the sample bias ( $V_s$ ) illustrating that  $\Delta h$  decreases with increasing  $V_s$ . Each data point is extracted from one single STM image so that the  $\Delta h$  of various  $A$ - $B$  pairs is measured under the same tip condition and imaging parameters.

freestanding oxide monolayer and the substrate lattices (16%), the efficient release of strain due to film rumpling enables the elastic term (unfavorable for adhesion) to remain roughly a third of the strength of the oxide-metal interaction term.

### C. Electronic structure and charge redistribution at the interface

The substrate-induced changes of the electronic structure can be best assessed via modifications of the cation magnetic

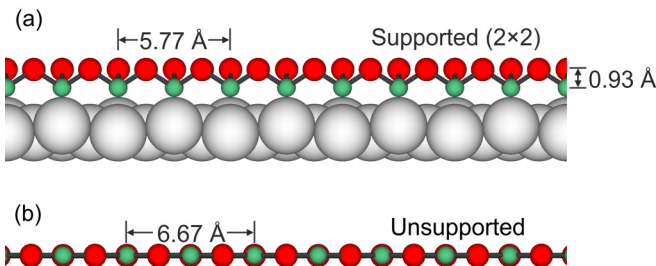


FIG. 4. Side views of the calculated structures of (a) Au(111)-supported and (b) freestanding  $\text{Nb}_2\text{O}_3$  films. Nb atoms are shown in green, O atoms are shown in red, and Au atoms are shown in gray.

moments  $\mu_{\text{Nb}}$ , charges  $Q_{\text{Nb}}$ , and the local density of states (LDOS) with respect to the freestanding reference monolayer.

The freestanding flat  $\text{Nb}_2\text{O}_3$  honeycomb monolayer is a Mott-Hubbard semiconductor with purely cationic states at the top of the valence band and at the bottom of the conduction band [Fig. 5(a)]. The Fermi level is located in the half-filled majority band of  $d_{xz} + d_{yz}$  character, in agreement with Ref. [21]. The filled majority  $d_{z^2}$  state, which contains the second valence electron of the  $\text{Nb}^{3+}$  cation, is located about 1 eV below the Fermi level. While the Bader charge  $Q_{\text{Nb}} = 1.61 e$  does not straightforwardly represent the  $\text{Nb}^{3+}$  formal charge, the cation magnetic moment  $\mu_{\text{Nb}} = 1.89 \mu_B$  is very close to the expected formal  $+2 \mu_B$  value.

All these electronic characteristics are substantially different in the Au-supported  $\text{Nb}_2\text{O}_3$  monolayer. There is a well-pronounced depletion of the purely Nb  $d$  states at the top of the valence band, consistent with the reduced cation contrast in the filled-state STM images [Fig. 2(c)]. As shown in Fig. 5(b), due to the rumpled geometry of the supported film, the  $d_{z^2}$  component loses its atomic-like character and hybridizes with the rest of the Nb  $d$  band. A similar difference can also be seen in the  $d_{xz} + d_{yz}$  band, which is significantly larger. Both  $d_{z^2}$  and  $d_{xz} + d_{yz}$  states lose their spin-polarized character and are visibly depleted. The cation magnetic moment  $\mu_{\text{Nb}}$  is entirely quenched ( $\mu_{\text{Nb}} = 0 \mu_B$ ) and the cation



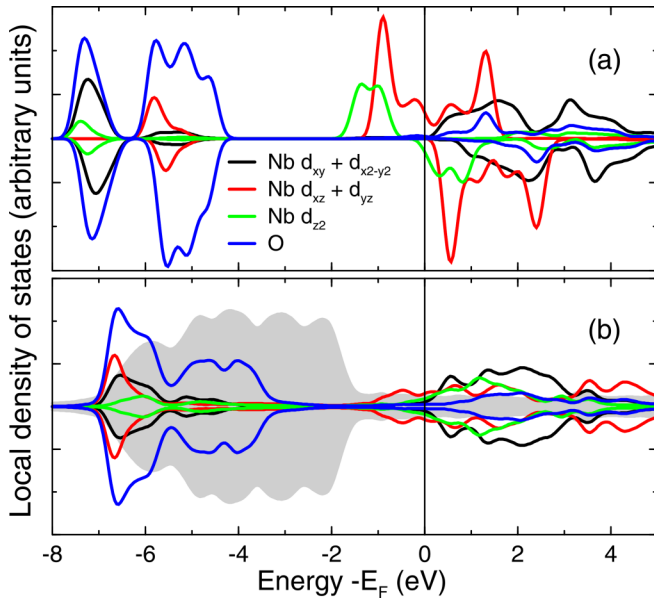


FIG. 5. Atom- and orbital- projected densities of states of (a) a freestanding and (b) a Au-supported  $\text{Nb}_2\text{O}_3$  honeycomb monolayer. A broadening of 0.2 eV has been systematically applied. The energy scales of the two systems are aligned by their Fermi levels. The gray LDOS in (b) is from the Au(111) substrate.

charge is increased by  $0.55 e$  ( $Q_{\text{Nb}} = 2.16 e$ ). These changes are associated with a particularly large electron transfer from the film towards the Au substrate,  $Q_{\text{Au}} = -1.28 e$  per  $\text{Nb}_2\text{O}_3$  unit. Although Bader charges and magnetic moments do not straightforwardly account for the formal oxidation states, the calculated changes are consistent with an increase of the Nb oxidation state from +3 in the freestanding film to +4/+5 in the supported one, with some uncertainty in their assignment due to the metallic character of the system. Similar changes in cation oxidation states have previously been reported in  $\text{Ti}_2\text{O}_3$  and  $\text{V}_2\text{O}_3$  honeycomb monolayers on Au(111) substrates [24].

The origin of such a large electron transfer can be traced back to the important offset between the Fermi levels of the separated systems: the freestanding film and the bare gold surface, whose calculated work functions are equal to 3.5 and 5.4 eV, respectively, within the present computational setup. Due to the relatively small electronegativity of niobium, the valence-band maximum in the freestanding honeycomb monolayer is located nearly 2 eV above the Fermi level of the gold substrate. Such a band misalignment is consistent with a depletion of the majority Nb  $d_{z^2}$  and  $d_{xz} + d_{yz}$  orbitals and an electron transfer towards the Au surface once the two systems are in contact, and was also invoked in other  $\text{M}_2\text{O}_3/\text{Au}$  systems [24].

As a consequence of this electron transfer, the gold surface becomes negatively charged and electrostatically repels (attracts) anions (cations), thus inducing positive film rumpling [41,42]. In calculations, we can allow a variation of the Au(111) in-plane lattice parameter in order to establish the lattice parameter energetically most favored by the supported oxide film. This enables us to establish the degree of compression or tension experienced by the monolayer due to the epitaxial match with the substrate [15]. The resulting

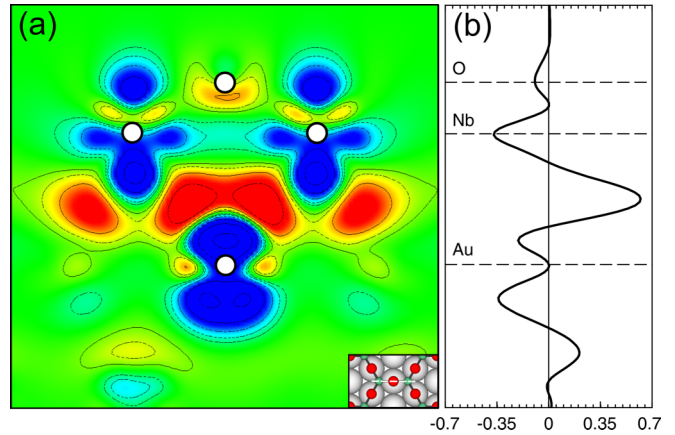


FIG. 6. (a) Difference electron density map in the supported  $\text{Nb}_2\text{O}_3$  honeycomb monolayer plotted in the plane perpendicular to the Au(111) surface and passing through two Nb, an oxygen, and a surface Au atom shown in the inset. Regions of electron excess and deficiency are depicted in red and blue, respectively. (b) Integrated differential density plotted along the direction perpendicular to the Au(111) surface.

$a \sim 6.1 \text{ \AA}$  ( $\delta z_{\text{Nb-O}} \sim 0.8 \text{ \AA}$ ) shows that the structural polarization induced by the charge transfer and the resulting reduction of the in-plane lattice parameter partially reduces the lattice mismatch with the gold substrate (5.77 Å). Hence the  $\text{Nb}_2\text{O}_3$  monolayer is in a state of in-plane elastic compressive strain of  $\sim 5.7\%$  ( $6.1 \text{ \AA} / 5.77 \text{ \AA}$ ).

As to better assess the spatial nature of the interfacial electron redistribution, Fig. 6 depicts the changes in the electron density at the  $\text{Nb}_2\text{O}_3/\text{Au}(111)$  interface. The map is obtained by subtracting the sum of total electron densities of the separated systems (the bare gold slab and the unsupported oxide film) from that of the constituted one (the oxide film deposited on the gold substrate), while maintaining all the atoms in the positions of the supported configuration. Positive (negative) difference densities correspond to regions which are populated with (depleted of) electrons upon the formation of the interface. The most visible effect is the accumulation of electrons in the interfacial region between the oxide film and the Au substrate and their localization along the cation-Au bonds (maxima of the electron density difference). These electrons originate mainly from the Nb cations, and from the surface Au atoms, which both display large negative difference densities, showing a well-pronounced depletion of principally their  $d_{z^2}$  orbitals. We note that the Bader decomposition of the charge density assigns the major part of the interfacial region to the Au surface, which results in a large negative charge ( $-1.28 e/\text{Nb}_2\text{O}_3$ ) of the metal substrate.

With respect to the bare Au(111) substrate, the change of work function  $\Delta W$  due to the presence of the oxide has three main contributions [42–44] due to: the compression of the gold electrons ( $\Delta W < 0$ ), the interface electron transfer from oxide to gold ( $\Delta W < 0$ ), and the rumpling of the oxide film ( $\Delta W > 0$ ). The small reduction of work function found in the calculations ( $\Delta W \sim -0.10 \text{ eV}$ ), despite the large rumpling of the supported oxide film, is due to a compensation between the structural and charge-transfer dipoles.

## V. CONCLUSION

A honeycomb ( $2 \times 2$ ) Nb<sub>2</sub>O<sub>3</sub> monolayer was successfully grown on a Au(111) substrate by Nb deposition and oxidation, and studied using STM, LEED, and DFT simulations. The results of our investigations show that the structure is stabilized by a particularly strong interaction between the Nb<sub>2</sub>O<sub>3</sub> film and the Au(111) substrate. It is accompanied by large interfacial electron transfer, a change of Nb oxidation state, and substantial film rumpling. The rumpling reduces the in-plane lattice parameter of the oxide monolayer compared with a freestanding film and thereby improves the lattice matching with the Au(111) substrate. Careful STM image processing using multiple frame averaging was able to discriminate be-

tween Nb fcc and hcp adsorption sites in qualitative agreement with the simulations. This two-dimensional oxide enriches the family of oxide monolayers of M<sub>2</sub>O<sub>3</sub> stoichiometry on metal substrates and raises the enticing prospect of the creation of mixed cation A<sub>x</sub>B<sub>2-x</sub>O<sub>3</sub> ( $0 \leq x \leq 2$ ) honeycomb structures.

## ACKNOWLEDGMENTS

We thank Chris Spencer (JEOL UK) for valuable technical support, Lewys Jones for assistance with image processing, and Xiao Hu for preliminary experimental investigations in this area.

- 
- [1] F. P. Netzer and A. Fortunelli (eds.), *Oxide Materials at the Two-Dimensional Limit*, Springer Series in Materials Science (Springer International Publishing, AG, Switzerland, 2016) Vol. 234.
- [2] S. Shaikhutdinov and H. J. Freund, *Annu. Rev. Phys. Chem.* **63**, 619 (2012).
- [3] H. Chen, M. Bettayeb, V. Maurice, L. H. Klein, L. Lapeire, K. Verbeken, H. Terryn, and P. Marcus, *Corros. Sci.* **111**, 659 (2016).
- [4] F. Sedona, G. A. Rizzi, S. Agnoli, F. X. Llabrés i Xamena, A. Papageorgiou, D. Ostermann, M. Sambì, P. Finetti, K. Schierbaum, and G. Granozzi, *J. Phys. Chem. B* **109**, 24411 (2005).
- [5] G. Barcaro, S. Agnoli, F. Sedona, G. A. Rizzi, A. Fortunelli, and G. Granozzi, *J. Phys. Chem. C* **113**, 5721 (2009).
- [6] G. Barcaro, E. Cavaliere, L. Artiglia, L. Sementa, L. Gavioli, G. Granozzi, and A. Fortunelli, *J. Phys. Chem. C* **116**, 13302 (2012).
- [7] M. S. J. Marshall and M. R. Castell, *Phys. Rev. Lett.* **102**, 146102 (2009).
- [8] F. Sedona, G. Granozzi, G. Barcaro, and A. Fortunelli, *Phys. Rev. B* **77**, 115417 (2008).
- [9] W. Steurer, S. Surnev, A. Fortunelli, and F. P. Netzer, *Surf. Sci.* **606**, 803 (2012).
- [10] N. Doudin, D. Kuhness, M. Blatnik, G. Barcaro, F. R. Negreiros, L. Sementa, A. Fortunelli, S. Surnev, and F. P. Netzer, *J. Phys. Chem. C* **120**, 28682 (2016).
- [11] F. Allegretti, G. Parteder, L. Gragnaniello, S. Surnev, F. P. Netzer, A. Barolo, S. Agnoli, G. Granozzi, C. Franchini, and R. Podloucky, *Surf. Sci.* **604**, 529 (2010).
- [12] S. Surnev, L. Vitali, M. G. Ramsey, F. P. Netzer, G. Kresse, and J. Hafner, *Phys. Rev. B* **61**, 13945 (2000).
- [13] C. Wu, M. S. J. Marshall, and M. R. Castell, *J. Phys. Chem. C* **115**, 8643 (2011).
- [14] C. Wu, M. R. Castell, J. Goniakowski, and C. Noguera, *Phys. Rev. B* **91**, 155424 (2015).
- [15] S. Wang, X. Hu, J. Goniakowski, C. Noguera, and M. R. Castell, *Nanoscale* **11**, 2412 (2019).
- [16] F. Tumino, P. Carrozzo, L. Mascaretti, C. S. Casari, M. Passoni, S. Tosoni, and C. E. Bottani, *2D Mater.* **2**, 045011 (2015).
- [17] D. Ragazzon, A. Schaefer, M. H. Farstad, L. E. Walle, P. Palmgren, A. Borg, P. Uvdal, and A. Sandell, *Surf. Sci.* **617**, 211 (2013).
- [18] M. H. Farstad, D. Ragazzon, L. E. Walle, A. Schaefer, A. Sandell, and A. Borg, *J. Phys. Chem. C* **119**, 6660 (2015).
- [19] S. Pomp, D. Kuhness, G. Barcaro, L. Sementa, V. Mankad, A. Fortunelli, M. Sterrer, F. P. Netzer, and S. Surnev, *J. Phys. Chem. C* **120**, 7629 (2016).
- [20] J. Goniakowski and C. Noguera, *J. Phys. Chem. C* **123**, 7898 (2019).
- [21] S. J. Zhang, C. W. Zhang, S. F. Zhang, W. X. Ji, P. Li, P. J. Wang, S. S. Li, and S. S. Yan, *Phys. Rev. B* **96**, 205433 (2017).
- [22] G. Kresse, S. Surnev, M. G. Ramsey, and F. P. Netzer, *Surf. Sci.* **492**, 329 (2001).
- [23] P. N. Plessow, M. Bajdich, J. Greene, A. Vojvodic, and F. Abild-Pedersen, *J. Phys. Chem. C* **120**, 10351 (2016).
- [24] J. Goniakowski and C. Noguera, *J. Phys. Chem. C* **123**, 9272 (2019).
- [25] C. Möller, H. Fedderwitz, C. Noguera, J. Goniakowski, and N. Nilius, *Phys. Chem. Chem. Phys.* **20**, 5636 (2018).
- [26] L. Jones, H. Yang, T. J. Pennycook, M. S. J. Marshall, S. Van Aert, N. D. Browning, M. R. Castell, and P. D. Nellist, *Adv. Struct. Chem. Imaging* **1**, 8 (2015).
- [27] L. Jones, S. Wang, X. Hu, S. ur Rahman, and M. R. Castell, *Adv. Struct. Chem. Imaging* **4**, 7 (2018).
- [28] See Supplemental Material at <http://link.aps.org/supplemental/10.1103/PhysRevB.100.125408> for details of the multiple frame averaging procedure using the SMART ALIGN software package.
- [29] J. P. Perdew and Y. Wang, *Phys. Rev. B* **45**, 13244 (1992).
- [30] G. Kresse and D. Joubert, *Phys. Rev. B* **59**, 1758 (1999).
- [31] G. Kresse and J. Hafner, *Phys. Rev. B* **49**, 14251 (1994).
- [32] G. Kresse and J. Furthmüller, *Phys. Rev. B* **54**, 11169 (1996).
- [33] J. Tersoff and D. R. Hamann, *Phys. Rev. Lett.* **50**, 1998 (1983).
- [34] R. F. W. Bader, *Chem. Rev.* **91**, 893 (1991).
- [35] G. Henkelman, A. Arnaldsson, and H. Jónsson, *Comput. Mater. Sci.* **36**, 354 (2006).
- [36] S. L. Dudarev, G. A. Botton, S. Y. Savrasov, C. J. Humphreys, and A. P. Sutton, *Phys. Rev. B* **57**, 1505 (1998).
- [37] J. Klimeš, D. R. Bowler, and A. Michaelides, *J. Phys.: Condens. Matter* **22**, 022201 (2010).

- [38] J. Klimeš, D. R. Bowler, and A. Michaelides, *Phys. Rev. B* **83**, 195131 (2011).
- [39] A. R. H. Clarke, J. B. Pethica, J. A. Nieminen, F. Besenbacher, E. Lægsgaard, and I. Stensgaard, *Phys. Rev. Lett.* **76**, 1276 (1996).
- [40] H. L. T. Le, J. Goniakowski, C. Noguera, A. Koltsov, and J. M. Mataigne, *J. Phys. Chem. C* **121**, 25143 (2017).
- [41] J. Goniakowski, C. Noguera, L. Giordano, and G. Pacchioni, *Phys. Rev. B* **80**, 125403 (2009).
- [42] J. Goniakowski and C. Noguera, *Phys. Rev. B* **79**, 155433 (2009).
- [43] L. Giordano, F. Cinquini, and G. Pacchioni, *Phys. Rev. B* **73**, 045414 (2006).
- [44] L. Giordano, G. Pacchioni, J. Goniakowski, N. Nilius, E. D. L. Rienks, and H.-J. Freund, *Phys. Rev. B* **76**, 075416 (2007).